Title
DERIVATION OF ONE-DIMENSIONAL REFRACTIVE-INDEX PROFILES FROM INTERFEROGRAMS

Authors
McLarnon, F.R.
Muller, R.H.
Tobias, C.W.

Publication Date
1975-04-01

Submitted to Journal of the Optical
Society of America

LBL-3141
Preprint

DERIVATION OF ONE-DIMENSIONAL REFRACTIVE-INDEX PROFILES FROM INTERFEROGRAMS

F. R. McLarnon, R. H. Muller, and C. W. Tobias

April 1975

Prepared for the U. S. Energy Research and
Development Administration under Contract W-7405-ENG-48

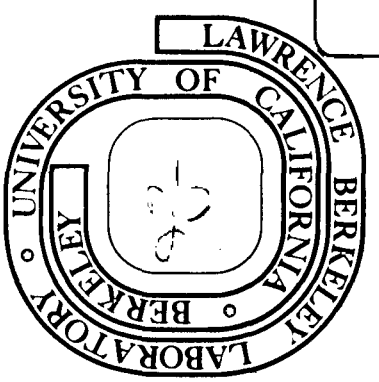

LBL-3141

DISCLAIMER

LBL-3141

DERIVATION OF ONE-DIMENSIONAL REFRACTIVE-INDEX PROFILES FROM INTERFEROGRAMS

F. R. McLarnon, R. H. Muller and C. W. Tobias

Inorganic Materials Research Division, Lawrence Berkeley Laboratory and Department of Chemical Engineering; University of California Berkeley, California 94720

ABSTRACT

A method is presented for the derivation of one-dimensional refractive-index fields from interferograms that may be distorted by light-deflection effects. The technique involves an iterative process that employs closed-form solutions for light-propagation through inhomogeneous media and a three-parameter polynomial function to describe the refractive-index field. The method was tested by analyzing the interferograms associated with various refractive-index fields generated by diffusion and convection at a solid-fluid interface. The results show that the derived polynomial refractive-index profiles closely approximate the concentration fields and accurately depict the interfacial refractive-index. However, the derived interfacial refractive-index gradient can be in error, because of the limitations in the precision with which the exact location of the interface can be established on an experimental interferogram.

Index Headings

Interferometry; Refraction; Refractive-index; Ray-tracing; Electrochemical boundary layers

Introduction

Conventional interpretation of interferograms assumes that light propagates along a straight line through a specimen. Local refractive-index variations within the specimen are then calculated from the local phase change (fringe shifts) in the interferogram.[1] However, because refractive-index variations normal to the beam direction deflect the beam as it traverses the refractive-index field, conventional interpretation of the resulting interferogram can lead to large errors.[2,3] This paper presents a method for the derivation of one-dimensional refractive-index profiles from interferograms which may be distorted by light-deflection effects.

A numerical solution to the equation of light deflection[2] has permitted computation of the interferogram associated with any given refractive-index field. For the reverse problem, an iterative technique must be used to calculate the refractive-index field associated with a given interferogram because no direct computational method exists. Closed-form solutions to the equation of light-deflection have now been derived for a polynomial-type refractive-index field and are used in the iterative method presented in this paper.

Light-Deflection in a Refractive-Index Field

Figure 1 schematically illustrates the trajectory of a light ray within a refractive-index field. The field in this case is a boundary layer, which is a transparent medium of variable refractive-index near an opaque surface (the plane identified by $y = 0$ in Fig. 1). The refractive-index increases continuously from its minimum value

n_s at $y = 0$ to its maximum value n_b at $y = \delta$, the edge of the boundary layer; and the refractive-index has a constant value n_b for $y \geq \delta$. Such boundary layers are encountered in heat and mass transfer between two phases. Local variations in temperature or concentration result in corresponding refractive-index variations near the interface. The trajectory $y(x)$ of light beam AB is calculated by solving the light-deflection equation for this coordinate system:[2,4]

$$\frac{d^2y}{dx^2} = \frac{1}{n}\left[1 + \left(\frac{dy}{dx}\right)^2\right]\left[\frac{\partial n}{\partial y} - \left(\frac{dy}{dx}\right)\frac{\partial n}{\partial x}\right] \qquad (1)$$

where $n = n(x,y)$ is the refractive-index within the field. Concurrently, the optical path length p of the beam must be calculated in order to determine the phase difference between various rays traversing the specimen:

$$p(x) = \int_0^x n(x,y)\sqrt{1 + \left(\frac{dy}{dx}\right)^2}\, dx \qquad (2)$$

Solution of the Light-Deflection Equations

In the analysis of one-dimensional boundary layers, the refractive-index is a function of y only ($n = n(y)$) and the last term on the right-hand side of Eq. (1) vanishes. Equation (1) may now be integrated directly:

$$\frac{dy}{dx} = \sqrt{\left(\frac{n}{n_e}\right)^2 - 1} \tag{3}$$

$$x = \int_{y_e}^{y} \frac{dy}{\sqrt{\left(\frac{n}{n_e}\right)^2 - 1}} \tag{4}$$

where y_e is the position where a particular light ray enters the specimen (parallel to the plane $y = 0$) and n_e is the medium refractive-index at $x = 0$ and $y = y_e$. The tractability of Eq. (4) depends upon the form of the refractive-index function $n = n(y)$. Solutions for a constant refractive-index gradient of unlimited extent ($n \propto y$) have been obtained previously.[1]

Solutions for more general refractive-index profiles can be obtained if the light-deflection equation [Eq. (4)] is simplified. If we define $\varepsilon = \frac{n}{n_e} - 1$, we see that ε is a small number for most practically observed concentration fields. For example, that maximum value of ε likely to be encountered in the interferometry of aqueous $CuSO_4$ systems[3] is about 0.01. We can then approximate $(n/n_e)^2 - 1 = 2\varepsilon + \varepsilon^2 \approx 2\varepsilon$ to within about 0.5%.

The light-deflection equations [Eqs. (2) to (4)] now simplify to

$$\frac{dy}{dx} = \sqrt{2\,\frac{n - n_e}{n_e}} \tag{5}$$

$$x = \int_{y_e}^{y} \frac{dy}{\sqrt{2\,\frac{n - n_e}{n_e}}} \tag{6}$$

$$p(x) = n_e \cdot x + 2 \int_0^x (n - n_e)dx \qquad (7)$$

Use of these approximate equations is justified in Appendix A for the interferometric analysis of a particular refractive-index field. Note that as $n \to n_e$, the refractive-index variations vanish and Eq. (7) becomes $p(x) = n_e \cdot x$, which corresponds to conventional interferogram interpretation.

Two-Parameter Refractive-Index Profile

A closed-form solution of both Eqns. (4) and (6) can be obtained (see Appendix B) for a parabolic refractive-index profile

$$\theta = \frac{n - n_s}{n_b - n_s} = 1 - (1 - Y)^2 = 2Y - Y^2 , \quad 0 \leq Y \leq 1 \qquad (8)$$

$$\theta = 1 , \quad Y \geq 1$$

where θ is a dimensionless refractive index and Y a dimensionless distance in a boundary layer $Y = y/\delta$. The parabolic profile has only two degrees of freedom, n_s and δ: the parameter n_s permits stretching along the refractive-index axis (e.g., the abscissa in Fig. 4) and the parameter δ allows stretching along the distance axis (e.g., the ordinate in Fig. 4).

Three-Parameter Refractive-Index Profile

A polynomial refractive-index function can be formulated as

$$\theta = 1 - (1 - kY)^2(1 - Y)^2 \ , \ -0.268 < k \leq 1 \ , \ 0 \leq Y \leq 1 \qquad (9)$$

$$\theta = 1 \ , \ Y \geq 1$$

where the limits on the parameter k insure that the function $\theta(Y)$ suffers no inflection or extremum points for $0 < Y < 1$. This relatively simple functionality offers two advantages: (a) it permits a closed-form solution to the equations of light-deflection [Eqs. (5) to (7)], and (b) it is flexible enough to closely approximate typical refractive-index fields encountered in heat and mass transfer. Note that the parabolic boundary layer profile Eq. (8) is a special case of Eq. (9) for $k = 0$.

There are three variable parameters in Eq. (9): n_s, δ and k. In addition to the two stretching parameters n_s and δ, the curve shape parameter k provides additional flexibility to fit data. The polynomial function Eq. (9) is plotted in Fig. 2 for several values of k.

We can obtain a closed-form solution to Eq. (6) for the polynomial boundary layer profile by first defining the following variables and parameters:

$$u(Y) = (1 - kY)(1 - Y) \qquad (10)$$

$$U = \frac{u}{u_e} = \frac{u(Y)}{u(Y_e)} \qquad (11)$$

$$m = \frac{1}{2}\left[1 + \frac{(1 - k)^2}{4k\ u_e}\right] \qquad (12)$$

$$h = 2\,\frac{n_b - n_e}{n_e} \tag{13}$$

$$x_m = \delta\sqrt{\frac{u_e}{2kh}} \tag{14}$$

U is a transformation variable related to dimensionless distance Y by

$$Y = \frac{1 + k}{2k} - \sqrt{\frac{u_e}{k}\,(2m - 1 + U)} \tag{15}$$

Using the new variable of integration U, Eq. (6) transforms into:

$$x = \frac{x_m}{\sqrt{2}} \int_U^1 \frac{dU}{\sqrt{(1 - U)(U + 1)(U - 1 + 2m)}} \tag{16}$$

for which the solution is:[5]

$$x = x_m \cdot sn^{-1}\left(\sqrt{\frac{1 - U}{2m}}\,,\ m\right) \tag{17}$$

where m (defined by Eq. (12)) is the parameter of the elliptic integral of the first kind sn^{-1}. Equation (17) can be inverted to a function of the Jacobian elliptic function sn:

$$U = 1 - 2m \cdot sn^2\left(\frac{x}{x_m}\,,\ m\right) \tag{18}$$

The phase integration formula Eq. (7) becomes:

$$p(x) = n_e\left[x + h\left(x - \int_0^x U^2 dx\right)\right] \tag{19}$$

which can be easily integrated by standard formulae (e.g., Gauss-Legendre Quadrature). Formulae similar to Eqs. (17) - (19) can be derived[6] for $k < 0$. For $k = 0$, the parabolic boundary layer formulae (see Appendix I) apply.

Calculation of Ray Trajectories and Optical Paths

Equation (18) may be used to calculate the trajectory of a light ray through a boundary layer. Figure 3 illustrates two types of ray trajectories to consider: Type I, represented by line ABC, in which the ray remains within the boundary layer for $0 \leq x \leq w$, and Type II, represented by line DEF, in which the ray leaves the boundary layer before entering the glass wall at $x = w$. Since the ray would leave the boundary layer by definition when the ray reaches the edge of the boundary layer $Y = 1$ (or $U = 0$), we can easily determine the type trajectory (I or II) of a ray by using Eq. (17) for $U = 0$ to calculate the abscissa location x_b where the ray leaves the boundary layer:

$$x_b = x_m \cdot sn^{-1}\left(\sqrt{\frac{1}{2m}}\,,\ m\right) \tag{20}$$

Type I $x_b > w$: the ray remains within the boundary layer for $0 \leq x \leq w$. Integration of Eq. (19) provides the optical path length of the beam:

$$p(x = w) \equiv p(w) = n_e\left[w + h\left(w - \int_0^w U^2 dx\right)\right] \tag{21}$$

The integral in Eq. (21) can be accurately evaluated by 3-point Gauss-Legendre Quadrature,[7] where Eq. (18) supplies the functional values $U^2(x)$. The accuracy of the 3-point quadrature is discussed in Appendix A. Eq. (18) and Eq. (15) provide the location $y(w)$ (see Fig. 1) of the ray as it leaves the medium to enter the glass wall. Equation (9) gives the medium refractive-index and Eq. (5) gives the slope of the ray at this plane.

Type II $x_b < w$: the ray leaves the boundary layer before entering the glass sidewall. For $x > x_b$, the ray travels along a straight line since above the edge of the boundary layer there is no refractive-index gradient. Inspection of Eqs. (5) and (13) shows that the ray has a slope $\frac{dy}{dx} = \sqrt{h}$ for $x_b \leq x \leq w$, so the location of the ray at the plane where it leaves the medium to enter the glass wall is

$$Y(w) = 1 + \sqrt{h}\ (w - x_b) \tag{22}$$

The optical path length of the ray can be calculated from Eq. (2) and Eq. (19):

$$p(w) = n_e\left[x_b + h\left(x_b - \int_0^{x_b} U^2 dx\right)\right] + n_b \cdot (w - x_b)\sqrt{1 + h} \tag{23}$$

Calculation of Interferograms from Known Refractive-Index Fields

The formulae derived in the previous section provide the trajectory $y(x)$ and the optical path length $p(x)$ of a light ray as it traverses the medium $0 \leq x \leq w$. The ray then passes through the glass wall $w \leq x \leq w + d$ and propagates to the imaging objective lens of the interferometer. If the real plane of focus (optically conjugate to the film plane of the interferometer) lies at some plane $x = x_f$, we can calculate[2] the location of the virtual plane of focus GM (Fig.1) (relative to the plane of light-exit $x = w + d$ from the specimen):

$$F = \frac{w - x_f}{n_b} + \frac{d}{n_g} \qquad (24)$$

The distance F is shown on Fig. 1 for focus at $x_f = 0$, $n_b = 1.33$ and $n_g = 1.5$. All rays, provided they are accepted by the objective lens, appear to emanate from the virtual plane of focus GM. The deflected ray ABC thus appears to come from its virtual origin M, and its location on the interferogram can be calculated by considering refraction in the glass wall and the distance $S = F \cdot \tan \phi_a$ shown in Fig. 1

$$y_i = y(w) + d \cdot \tan \phi_g - F \cdot \tan \phi_a \qquad (25)$$

The angles ϕ_g in the glass wall and ϕ_a in the surrounding medium (e.g., air) are easily determined by Snell's Law.

Phase on the interferogram is calculated from the optical path length difference between the deflected ray ABC (Fig. 1) and a hypothetical undeflected ray LMN passing (in bulk solution) through the virtual origin M. The exit points C and N of each ray lie on an equiphase arc CN centered on the virtual origin M. Beyond points C and N the imaging optics introduce no phase difference between the rays ABC and LMN. The optical path p_o of the hypothetical undeflected ray is calculated by considering the distance $T = F\cdot\left(\sqrt{1 + \tan^2 \phi_a} - 1\right)$ on Fig. 1:

$$p_o = n_b\cdot w + n_g\cdot d + F\cdot\left(\sqrt{1 + \tan^2 \phi_a} - 1\right) \qquad (26)$$

where the surrounding medium is assumed to be air. The optical path difference between a deflected ray ABC (Fig. 1) and the undeflected ray LMN of the same virtual origin is given by

$$\Delta p = p(w) + n_g\cdot d\cdot \sqrt{1 + \tan^2 \phi_g} - p_o \qquad (27)$$

and is related to the number of fringe shifts on the interferogram by

$$N = \left|\frac{\Delta p}{\lambda}\right| \qquad (28)$$

Using a large number (e.g., 50) of rays entering the plane $x = 0$ at different positions (y_e values) an interferometric phase vs distance relationship, i.e. an interferogram, can be constructed by application of the above formulae.

Derivation of Refractive-Index Profiles from Interferograms

Although the interferogram associated with a given polynomial refractive-index field can now be derived in closed form, the reverse is not possible. Rather, an iterative technique is required to find the refractive-index profile associated with a given (i.e., experimental) interferogram. The three variable parameters of the polynomial function Eq. (9) can be estimated by a conventional analysis of the interferogram. These parameters are then varied in a systematic fashion, and a new interferogram is calculated each time a single parameter is changed until the best fit between the experimental and computed interferograms is found.

The following parameter variation technique has been used to find the refractive-index profile associated with a given interferogram by minimizing the deviations between the given and calculated interferograms:

1. Vary the interfacial refractive-index n_s until the average deviation between computed and given interferograms is zero (or less than some arbitrary small value).
2. Change the orientation parameter k and calculate the new n_s value by repeating step #1.
3. Repeat step #2 until a minimum in standard deviation between calculated and given interferograms is found.
4. Change the boundary layer thickness δ and calculate the new k and n_s values by repeating step #3.

5. Repeat step #4 until a minimum in standard deviation between calculated and given interferograms is found.

Details of this iterative technique are given elsewhere.[6]

Accuracy of Polynomial Representation of Refractive-Index Fields

Results of sample interferogram analyses are shown in Fig. 4. On the abscissa of this figure the interference order (fringe shifts) is linearly related to refractive-index (concentration). [This relation corresponds to conventional interpretation $\Delta p = w(n - n_b)$]. The true refractive-index fields correspond to concentration profiles (boundary layers) formed by the electrodeposition of Cu from aqueous 0.1 M $CuSO_4$ electrolyte. These profiles are depicted by the filled circles on Fig. 4 and correspond to the following functional relationships:

$$\text{a:}\quad \theta = 1 + \pi^{1/2} Y(1 - \text{erf}Y) - e^{-Y^2} \tag{29a}$$

$$\text{b:}\quad \theta = \text{erf}Y \tag{29b}$$

$$\text{c:}\quad \theta = 2Y - 2Y^3 + Y^4 \ . \tag{29c}$$

Equations (29a) and (29b) describe the concentration profiles[3] formed by diffusion-controlled electrodeposition at (a) constant current[9] (constant interfacial refractive-index gradient) and (b) constant potential[10] (constant interfacial refractive-index). Equation (29c) describes a Pohlhausen-type field[11]; it approximates rather well the concentration profile one might expect[12] for forced convection-controlled

electrodeposition. The open circles shown on Fig. 4 are the "data" which define an interference fringe to be analyzed. These points were calculated by numerical integration[2,8] of the light-deflection equation (Eq. (1)) for the refractive-index fields Eq. (29) for real plane of focus $x_f = 0$. The solid and dashed curves are the derived polynomial concentration profile and its associated computed interferogram, respectively. 40-90 iterations are usually required to find the minimum standard deviation between computed (dashed curve) and given (open circles) interferograms, consuming about 1 sec of computer[13] time. About 20 seconds of computer time would be required to perform a similar analysis using a numerical solution[2,8] of the light-deflection equation.

Figure 4 shows that the refractive-index field derived from a given interferogram by the technique presented in this paper does approximate the true field. A serious question arises, however, about the uniqueness of the derived refractive-index profile. In Fig. 4b and 4c the form of the derived profile closely approximates the form of the true profile, but careful inspection shows that the slopes dC/dy at $y = 0$ do not match. Figures 5 and 6 present a series of computations that illustrate this problem. Figure 5 depicts the ratio R_g of the derived interfacial refractive-index gradient to the true interfacial refractive-index gradient as a function of the true gradient. The calculations were performed for the three model refractive-index profiles Eqs. (29) for a real plane of focus $x_f = 0$. The filled symbols on Fig. 5 represent conventional interpretation of the (computed) interferograms while the open symbols illustrate

interpretation as previously described in Fig. 4. Figure 6 shows similar calculations for the ratio R_n of derived refractive-index differences (bulk less interfacial) to the true refractive-index difference.

The open points in Figs. 5 and 6 show that while the technique presented here is likely to find the interfacial refractive-index to within 5%, serious (up to 30%) errors can result in the determination of the interfacial refractive-index gradient. These errors are related to the insufficient flexibility of the polynomial refractive-index function Eq. (9); it can accurately represent the model profile Eq. (29a), but it cannot adequately describe the profiles Eqns. (29b) and (29c).

Although one's immediate reaction might be to suggest another refractive-index functionality, more general than Eq. (9), careful inspection of Fig. 4 indicates a problem in the uniqueness of the refractive-index field derived from the interferogram. Note that the end-point of the computed interferogram (dashed line) matches the end point of the given interferogram (lowest open circle) only in Fig. 4a. In Fig. 4b and 4c, there are 0.023 mm and 0.017 mm discrepancies between the end points. This misfit is the only apparent signal that the best match between computed and given (experimental) interferograms has not been found. In practice, there is considerable difficulty[14] in reading the exact location of the interface on an experimental interferogram, so it is unlikely that this small difference between the computed and given interferograms could be detected. In other words, there are two different refractive-index fields (e.g. the

solid curve and filled circles in Fig. 4b) associated with practically indistinguishable interferograms (e.g., the dashed curve and open circles in Fig. 4b). Thus, while the technique presented in this paper can indeed approximate both the form of the refractive-index field and the interfacial refractive-index associated with a given interferogram, it is not able to find either the unique refractive-index profile functionality or the exact interfacial refractive-index gradient.

Under certain circumstances, however, it may be possible to determine the true refractive-index profile functionality directly from the (distorted) interferogram. The solid curves in Fig. 7 depict two specific forms of the polynomial refractive-index function Eq. (9): the parabolic profile $k = 0$ and the quartic profile $k = 1$, both in dimensionless form. The computed dimensionless interferograms associated with the parabolic and quartic profiles are indicated by the dashed curves. The close agreement between the form of the parabolic profile and its associated interferogram suggests that the true refractive-index functionality may be determined directly from the distorted interferogram if the true profile is not too different from parabolic. For example, the Pohlhausen profile Eq. (29c) would be of this type. However, the mismatch between the quartic profile and its associated interferogram suggests that the refractive-index functionality cannot be determined directly from the distorted interferogram. This is the case for the refractive-index functionality Eq. (29a).

The filled symbols in Figs. 5 and 6 show that except for small refractive-index gradients, conventional interpretation of interferograms can lead to large (up to 60-85%) errors in the determination of the interfacial composition and gradient of refractive-index. Reference (3) discusses the effect of specimen sizes and refractive-index differences on such light-deflection errors. While the technique presented in this paper obviously has its limitations, it is certainly preferable to the conventional interpretation of interferograms when the refractive-index gradients are large.

Determination of the unique refractive-index field associated with a given interferogram is possible only if at least one of the following conditions is met:

(1) If the refractive-index gradients are so small that light-deflection effects are negligible.

(2) If the light-deflection equation can be inverted and the refractive-index field directly determined from the interferogram.

(3) If the form of the refractive-index function is known beforehand,[15] numerical integration of the light-deflection equation coupled with a suitable iteration technique can be used to determine quantities such as interfacial refractive-index, etc.

(4) If, for example, the interfacial refractive-index gradient is known beforehand,[16] numerical integration of the light-deflection equation can be performed for various types of refractive-index profiles until the derived gradients match the known gradients.

(5) If the refractive-index functionality is not unlike the parabolic profile k = 0, the functionality may be determined directly from the interferogram.

ACKNOWLEDGEMENT

This work was performed under the auspices of the U. S. Energy Research and Development Administration.

Appendix I

Parabolic Refractive Index Profile

The solution to the complete equation of light-deflection [Eq. (4)] can be obtained for a parabolic refractive-index profile Eq. (8) by use of the following transformation:

$$H = \frac{n}{n_e} \quad \text{and} \quad H_{max} = \frac{n_b}{n_e} \tag{30}$$

In addition, a scaling factor x_p is defined as

$$x_p = \delta\sqrt{\frac{n_e}{(n_b - n_s)(1 + H_{max})}} \tag{31}$$

Eq. (4) then transforms into

$$x = \frac{\delta}{2}\sqrt{\frac{n_e}{n_b - n_s}} \int_1^H \frac{dH}{\sqrt{(H_{max} - H)(H - 1)(H + 1)}} \tag{32}$$

for which the solution is[5]

$$x = x_p \cdot sn^{-1}\left(\sqrt{\frac{1}{m}\frac{H - 1}{H + 1}}\ ,\ m\right) \tag{33}$$

Here, m is the parameter for the elliptic integral of the first kind sn^{-1} and is defined as $m = (n_b - n_e)/(n_b + n_e)$ for this solution. Equation (33) may be inverted:

$$H = \frac{1 + m \cdot sn^2\left(\frac{x}{x_p}, m\right)}{1 - m \cdot sn^2\left(\frac{x}{x_p}, m\right)} \tag{34}$$

where sn is the Jacobian elliptic function, and the phase integration equation [Eq. (2)] becomes:

$$p(x) = n_e \cdot \int_0^x H^2 dx \tag{35}$$

which may be integrated by standard formulae (e.g., Gauss-Legendre Quadrature).

The simplified form of the light-deflection equations [Eqs. (6) and (7)] can be integrated directly for a parabolic boundary layer profile:

$$\frac{Y - 1}{Y_e - 1} = \cos \frac{x}{x_0} \tag{36}$$

$$p(x) = n_b \cdot x - (n_b - n_e) \cdot x_0 \cdot \sin \frac{x}{x_0} \cdot \cos \frac{x}{x_0} \tag{37}$$

where

$$x_0 = \delta \sqrt{\frac{n_e}{2(n_b - n_s)}} \tag{38}$$

Equation (37) is a closed-form solution of the phase integration equation and can be used to estimate the accuracy of Gauss-Legendre

quadrature as applied to Eqs. (35) and (37). Equation (36) permits a simple determination of the location x_b where all rays leave the boundary layer:

$$x_b = \frac{\pi}{2} x_0 \, . \tag{39}$$

Appendix II

Validity of Approximations

The effect of the approximations made in the derivation of the closed-form solutions of the light-deflection equations (Eqs. 17, 19, 33 and 37) has been investigated by computing interferograms for a type I and a type II boundary layer, using different computation schemes. Two parabolic boundary layers are chosen to represent an electrochemical system[3,6,8] where the refractive-index field corresponds to aqueous $CuSO_4$ electrolyte depleted in $CuSO_4$ concentration near an electrode surface. For each case, the concentration difference between the bulk ($y \geq \delta$) solution and the interface ($y = 0$) is 0.1 M $CuSO_4$, corresponding to refractive-index values[3] $n_b = 1.3340$ and $n_s = 1.3311$ at $\lambda = 632.8$ nm.

Type I: $\delta = 0.70$ mm, and no rays are deflected out of the boundary layer.

Type II: $\delta = 0.35$ mm, and all rays are deflected out of the boundary layer.

Two characteristics of the computed interferograms are given in Table I: y_{sf}, the position on the interferogram of a ray entering the specimen at $y_e = 0$; and ΔN, the total number of fringe shifts seen on the interferogram. The calculations are performed for w = 10.0 mm, d = 12.7 mm and λ = 632.8 nm (see Ref. 2 for the dependence of light-deflection errors on w, d and $n_b - n_s$).

The accuracy of the phase integration by 3-point Gauss-Legendre Quadrature can be checked by comparing computations #3 and #4 of Table I. Both computations have been carried out for the simplified version of the light-deflection equation [Eq. (6)], but the calculation scheme #4 uses the Gauss-Legendre Quadrature while #3 uses the closed-form solution for the phase integration, Eq. (37).

The accuracy of approximating Eqs. (4) and (2) with Eqs. (6) and (7) can be checked by comparing scheme #4 with scheme #2. Note that the approximation is good to within 0.1%.

The accuracy of the numerical integration[2,8] of the light-deflection equation can be checked by comparing schemes #5-9 with #2. Note that about 500 intervals (step size 0.02 mm) are required to approach the closed-form solution to within 0.001 mm (y_{sf}) and 0.1 fringe (ΔN).

Table I

Validity of Approximations and Convergence of Numerical Solutions

Computation Scheme #			Type I boundary layer δ = 0.70 mm		Type II boundary layer δ = 0.35 mm	
			y_{fs} (mm)	ΔN (number of fringes)	y_{fs} (mm)	ΔN (number of fringes)
1	Conventional analysis Eq. 29		0	45.83	0	45.83
2	Eqs. 33 - 35*		-0.2466	53.26	-0.2027	38.51
3	Eqs. 36 - 37		-0.2464	53.25	-0.2025	38.50
4	Eq. 36*		-0.2464	53.25	-0.2025	38.50
	Numerical Integration[2,8]					
	Intervals	Mesh Size (mm)				
5	10	1.0	-0.2824	57.20	-0.2663	47.42
6	100	0.1	-0.2502	53.66	-0.2086	39.00
7	500	0.02	-0.2474	53.35	-0.2039	38.68
8	1000	0.01	-0.2469	53.29	-0.2035	38.62
9	10000	0.001	-0.2467	53.26	-0.2030	38.54

*3-point Gauss-Legendre Quadrature used for phase integration

REFERENCES

1. R. H. Muller, in Advances in Electrochemistry and Electrochemical Engineering, R. H. Muller, ed. (Wiley-Interscience, New York, 1973) Vol. 9, pp. 326-353.
2. K. W. Beach, R. H. Muller and C. W. Tobias, J. Opt. Soc. Am. 63, 559 (1973).
3. F. R. McLarnon, R. H. Muller and C. W. Tobias, J. Electrochem. Soc. 122, 59 (1975).
4. F. P. Kapron, J. Opt. Soc. Am. 60, 1433 (1970).
5. M. Abramowitz and I. Stegun, eds., Handbook of Mathematical Functions, Washington, National Bureau of Standards, 1964, pp. 569-607.
6. F. R. McLarnon, Ph. D. Thesis, LBL-3500, Department of Chemical Engineering, University of California, Berkeley, Dec. 1974.
7. L. Lapidus, Digital Computation for Chemical Engineers, (McGraw-Hill, New York, 1962) p. 60.
8. K. W. Beach, Ph.D. Thesis, UCRL-20324, Dept. of Chemical Engineering, University of California, Berkeley (Univ. Microfilms, Ann Arbor, Michigan, order no. 72-13269).
9. H. J. S. Sand, Phil. Mag. (6) 1, p. 45 (1901).
10. F. G. Cottrell, Z. Physikal. Chem. 42, 385 (1903).
11. H. Schlichting, Boundary Layer Theory, (McGraw-Hill, New York, 1968) p. 291.
12. J. S. Newman, Ind. and Eng. Chem. 60, 12 (1968).
13. Control Data Corporation 7600 computer.
14. A 0.1° misalignment of the test beam corresponds to a 0.02 mm uncertainty in the location of a 10 mm wide surface.

15. This is the case for diffusion-controlled electrodeposition. See Ref. (3).

16. In many electrochemical systems, the local interfacial refractive index gradient is directly related to local current density, which can often be measured independently.

NOMENCLATURE

C	electrolyte concentration (M $CuSO_4$)
d	glass wall width (mm)
F	location of virtual plane of focus (mm)
h	parameter Eq. (13)
H, H_{max}	transformation variable Eq. (30)
i	current density (mA cm^{-2})
k	parameter Eq. (9)
m	parameter of the elliptic integral of the first kind Eq. (12) or Eq. (33)
n	refractive-index
n_b	bulk refractive-index ($y \geq \delta$)
n_e	refractive-index at $x = 0$, $y = y_e$
n_s	interfacial refractive-index ($y = 0$)
N	interference order Eq. (28)
p	optical path length (mm)
p_o	optical path length of undeflected ray (mm)
R_g	ratio of the derived interfacial refractive-index gradient to the true gradient
R_n	ratio of the derived refractive-index difference $n_b - n_s$ to the true difference
u	transformation variable Eq. (10)
u_e	$u(y_e)$
U	u/u_e
w	cell width (mm)
x	horizontal distance (mm)

x_b	location where ray leaves boundary layer (mm) (Eqs. (20), (39))
x_m	parameter (mm) Eq. (14)
x_0	parameter (mm) Eq. (38)
x_p	parameter (mm) Eq. (31)
y	vertical distance (mm) Fig. 1
y_e	position of light entrance into specimen (mm) Fig. 1
y_i	distance on interferogram (mm)
y_{sf}	interfacial location on interferogram (mm)
Y	dimensionless distance $Y = y/\delta$
Y_e	y_e/δ
δ	boundary layer thickness (mm)
ΔN	number of fringe shifts on an interferogram
Δp	optical path difference (mm)
ε	$(n - n_e)/n_e$
θ	dimensionless refractive-index Eq. (8), (9), or (29)
λ	wavelength of light (nm)
ϕ_a	ray angle in air (rad)
ϕ_g	ray angle in glass (rad)

FIGURE CAPTIONS

Fig. 1. Schematic illustration of a light ray trajectory.

ABC Ray trajectory

LMN Hypothetical undeflected ray

GM Virtual plane of focus

CN Equiphase arc centered on virtual origin M

PQ Edge of the boundary layer

x Horizontal distance

y Vertical distance

y_e Position of light ray entrance into specimen

d Glass wall thickness, refractive-index n_g

w Cell thickness, medium refractive-index $n(x,y)$

F,S,T See text

δ Boundary layer thickness

Fig. 2. Polynomial boundary layer refractive-index profiles.

Ordinate: dimensionless distance $Y = y/\delta$

Abscissa: dimensionless refractive-index $\theta = (n-n_s)/(n_b-n_s)$

a $k = -0.268$

b $k = 0$

c $k = 0.5$

d $k = 1.0$

Fig. 3. Schematic illustration of different ray trajectories.

ABC Trajectory of a ray that remains inside the boundary layer (Type I)

DEF Trajectory of a ray that is deflected out of the boundary layer (Type II)

GH Edge of the boundary layer

Fig. 4. Interpretation of interferograms.

Abscissa: local concentration (M $CuSO_4$) or phase change N (fringes).

Ordinate: distance y(mm).

O O O Interferogram (phase vs distance relationship) to be analyzed. (Computed from the refractive-index fields (Eq. (29)) by numerical methods[2,8].) Plane of focus $x_f = 0$, $w = 10.0$ mm and $d = 12.7$ mm .

——— Polynomial concentration profile (refractive-index field) derived from the above interferogram.

- - - Interference fringe associated with the above concentration profile.

o o o o True concentration profile (refractive-index field Eq. 29). $C_s = 0$ and $C_b = 0.1$ M $CuSO_4$ ($n_s = 1.3311$ and $n_b = 1.3340$ for $\lambda = 632.8$ nm).

a Refractive-index field described by Eq. (29a). Derived concentration profile: $\delta = 0.535$ mm, $k = 0.800$, $C_s = -0.0004$ M $CuSO_4$. Standard deviation 1.97×10^{-4} M $CuSO_4$ per data point.

b Refractive-index field described by Eq. (29b). Derived concentration profile: $\delta = 0.408$ mm, $k = 0.454$, $C_s = -0.0053$ M. Standard deviation 2.43×10^{-4} M/point.

c Refractive-index field described by Eq. (29c). Derived concentration profile: δ = 0.272 mm, k = 0.068, C_s = -0.0020 M. Standard deviation 1.37 X 10^{-4} M/point.

Fig. 5. Relative error of measured interfacial refractive-index gradients.

Abscissa: true interfacial refractive-index gradient (cm^{-1}).

Ordinate: R_g = derived interfacial refractive-index gradient divided by true gradient.

○ ▽ □ Apparent refractive-index gradient derived by conventional interpretation of the (computed) interferograms.

○ ▽ □ Refractive-index gradient derived by interpretation of interferograms as shown in Fig. 4.

○ ○ Refractive-index field described by Eq. (29a).

▽ ▽ Refractive-index field described by Eq. (29b).

□ □ Refractive-index field described by Eq. (29c).

Fig. 6. Relative error of measured interfacial refractive-index.

Abscissa: true interfacial refractive-index gradient (cm^{-1}).

Ordinate: R_n = derived refractive-index difference ($n_b - n_s$) divided by true refractive-index difference.

○ ▽ □ Apparent interfacial refractive-index derived by conventional interpretation of the (computed) interferograms.

○ ▽ □ Interfacial refractive-index derived by interpretation of interferograms as shown in Fig. 4.

Other designations as in Fig. 5.

Fig. 7. Parabolic and Quartic refractive-index fields and corresponding interferograms.
Ordinate: dimensionless distance

Abscissa: dimensionless refractive-index

———— True refractive-index field (parabolic $k = 0$ and quartic $k = 1$).

- - - - - Computed interferogram associated with the true refractive-index field. Corresponds to interfacial refractive-index gradient $\left.\frac{dn}{dy}\right|_{y=0} = 0.3\ cm^{-1}$.

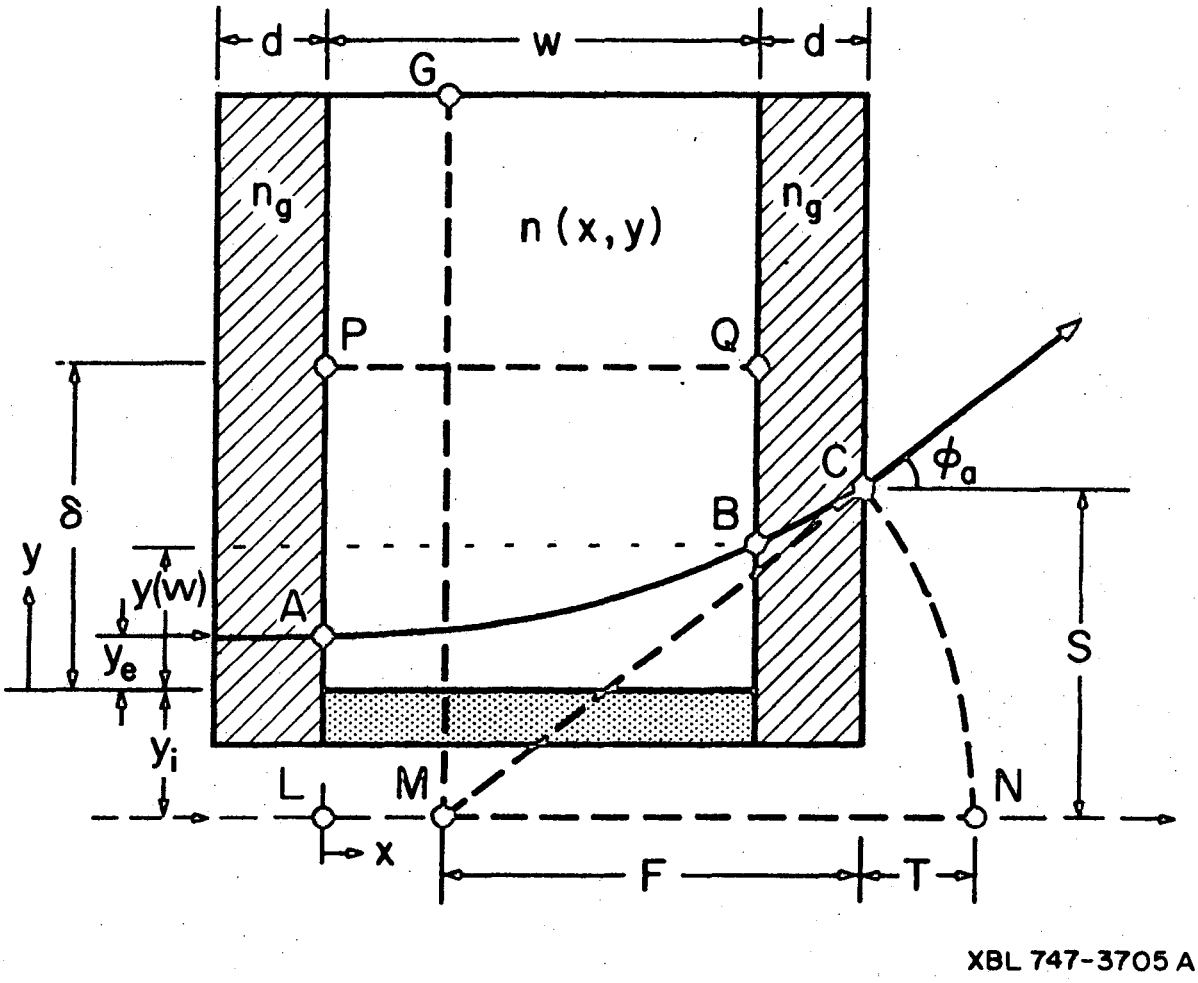
d
w
d
G
n_g
n (x, y)
n_g
P
Q
C
ϕ_a
δ
B
y
y(w)
A
y_e
S
y_i
L
M
N
x
F
T
XBL 747-3705 A

Fig. 1

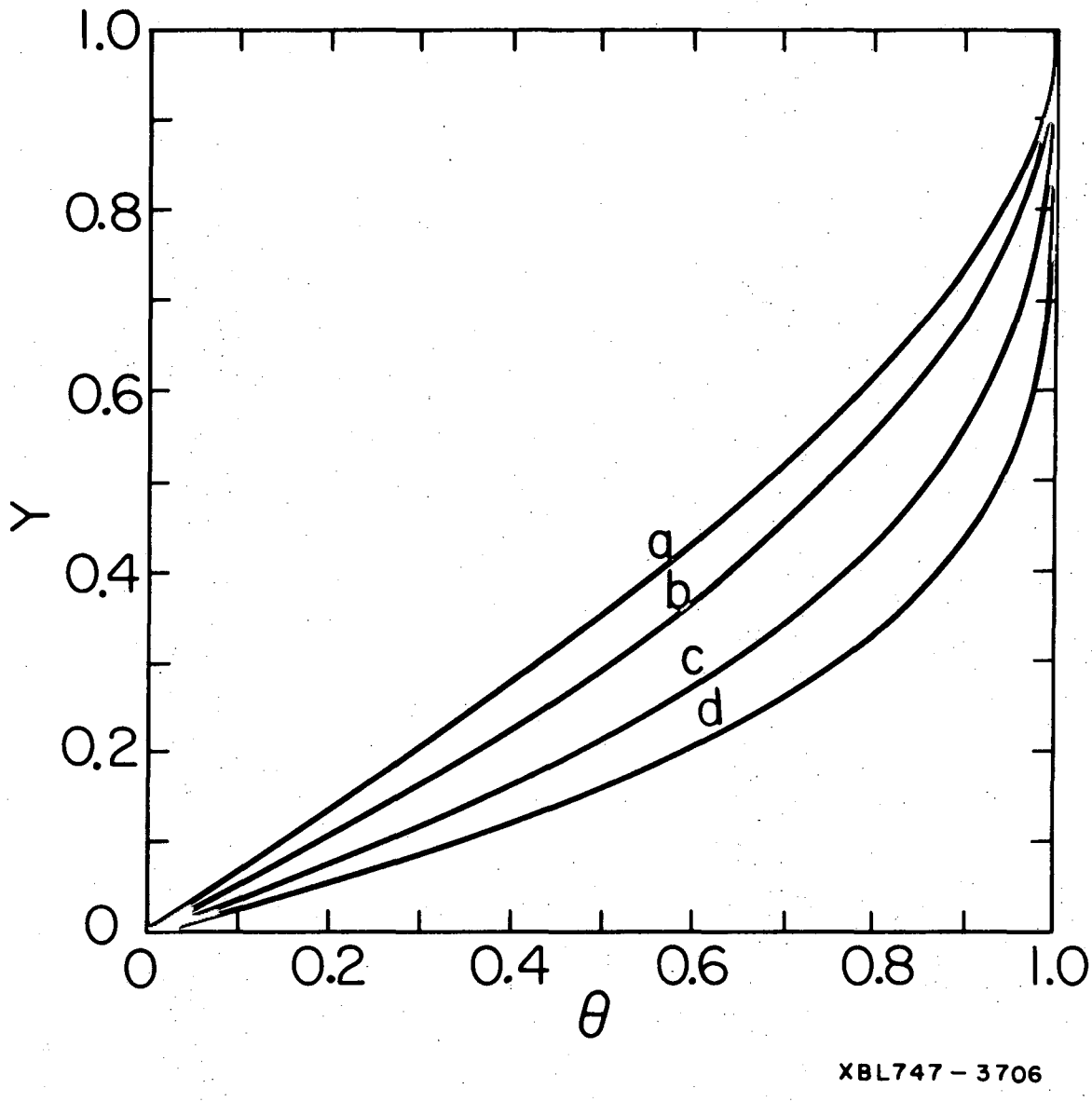

Fig. 2

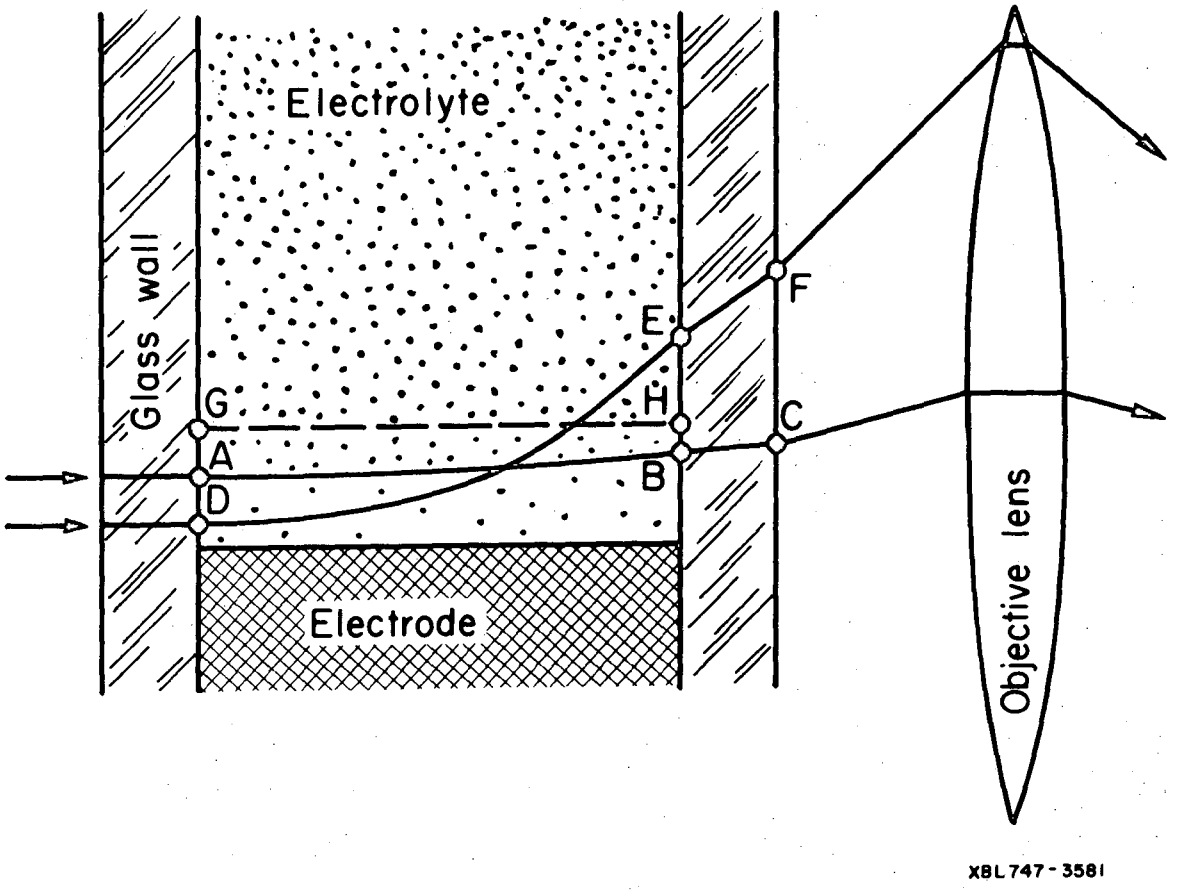
Electrolyte
Glass wall
Electrode
Objective lens
A
B
C
D
E
F
G
H
XBL747-3581

Fig. 3

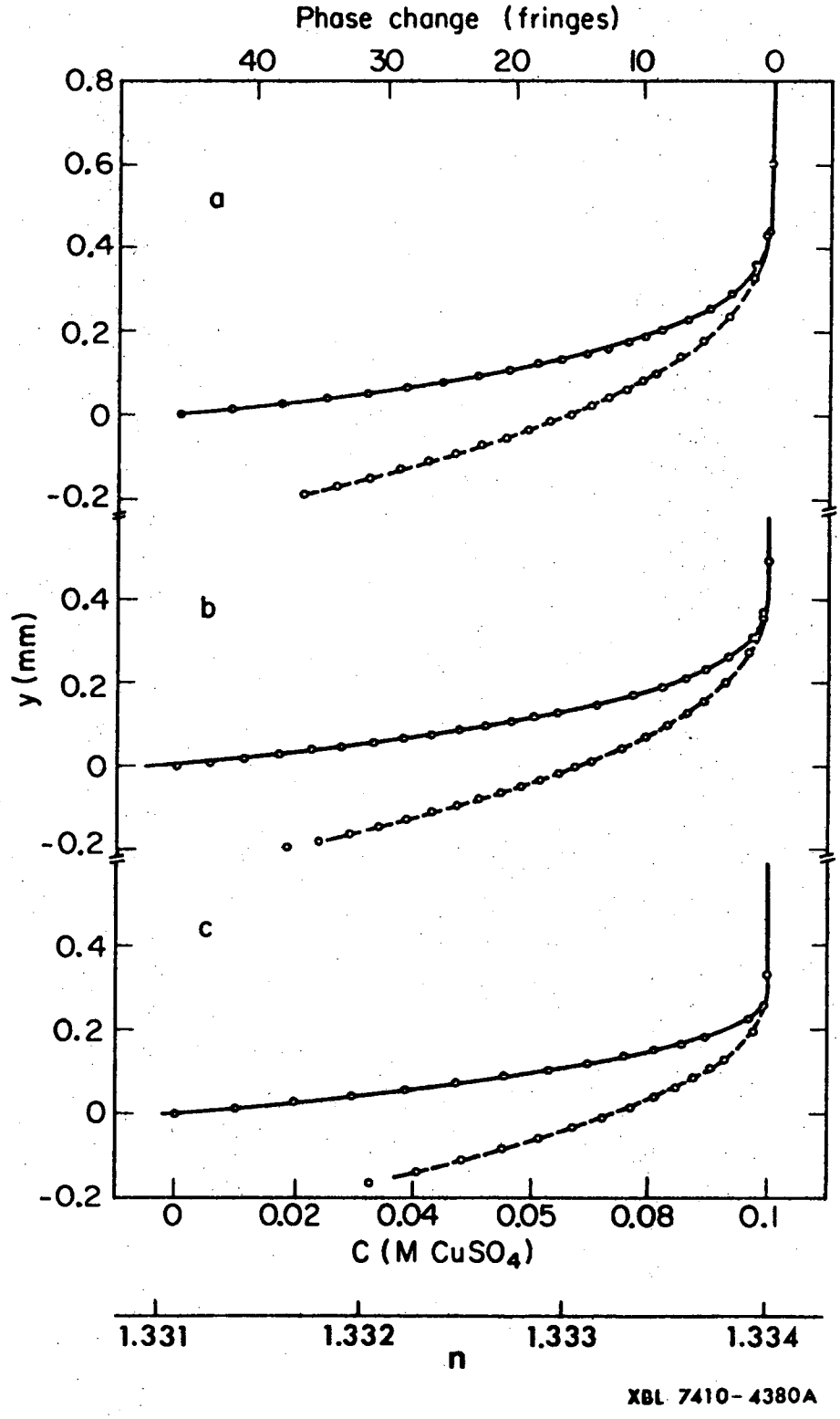
Phase change (fringes)
40
30
20
10
0
0.8
0.6
0.4
0.2
0
-0.2
a
b
c
y (mm)
0
0.02
0.04
0.05
0.08
0.1
C (M CuSO4)
1.331
1.332
1.333
1.334
n
XBL 7410-4380A

Fig. 4

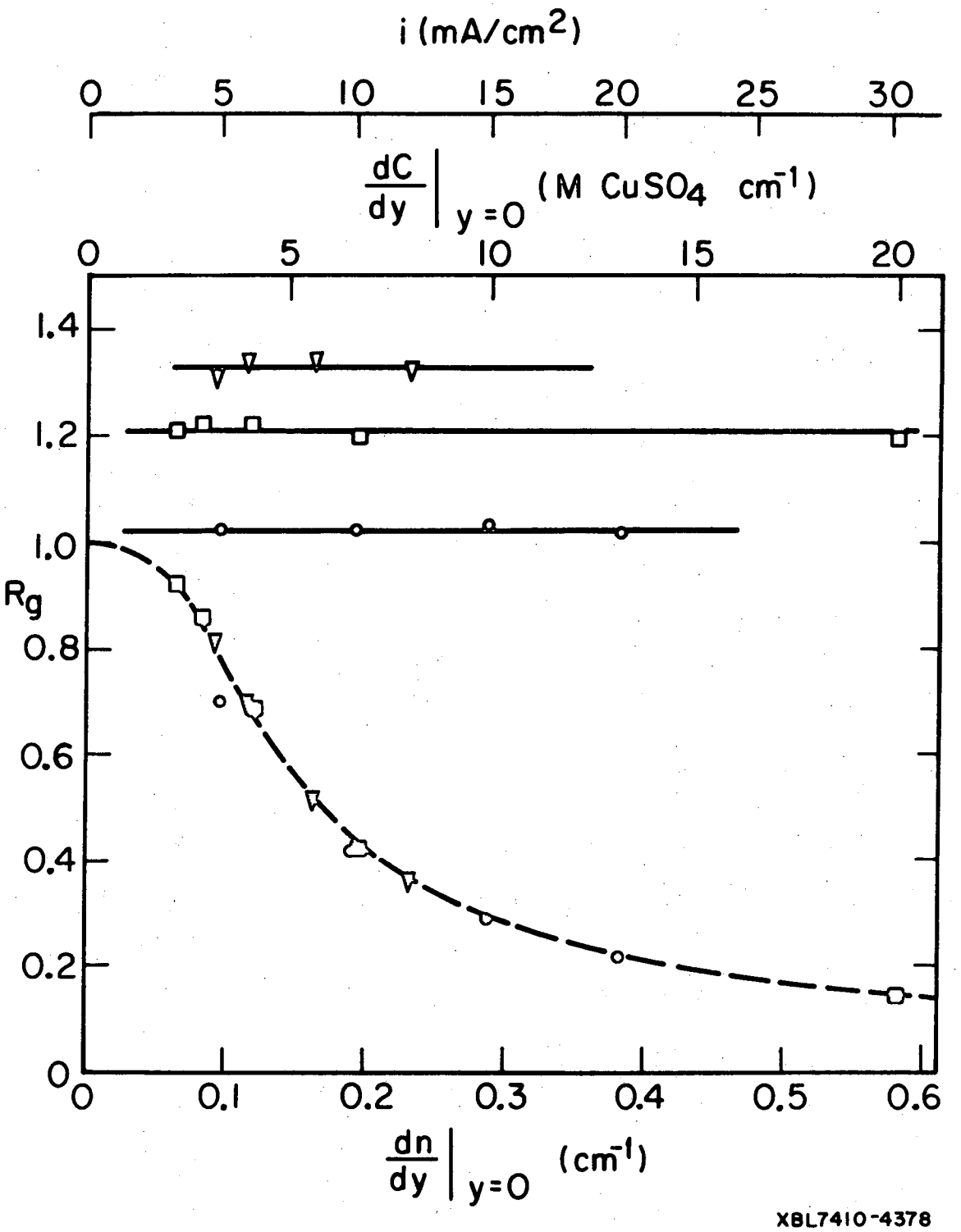
i (mA/cm²)
0
5
10
15
20
25
30
dC/dy | y=0 (M CuSO4 cm⁻¹)
0
5
10
15
20
1.4
1.2
1.0
Rg
0.8
0.6
0.4
0.2
0
0
0.1
0.2
0.3
0.4
0.5
0.6
dn/dy | y=0 (cm⁻¹)
XBL7410-4378

Fig. 5

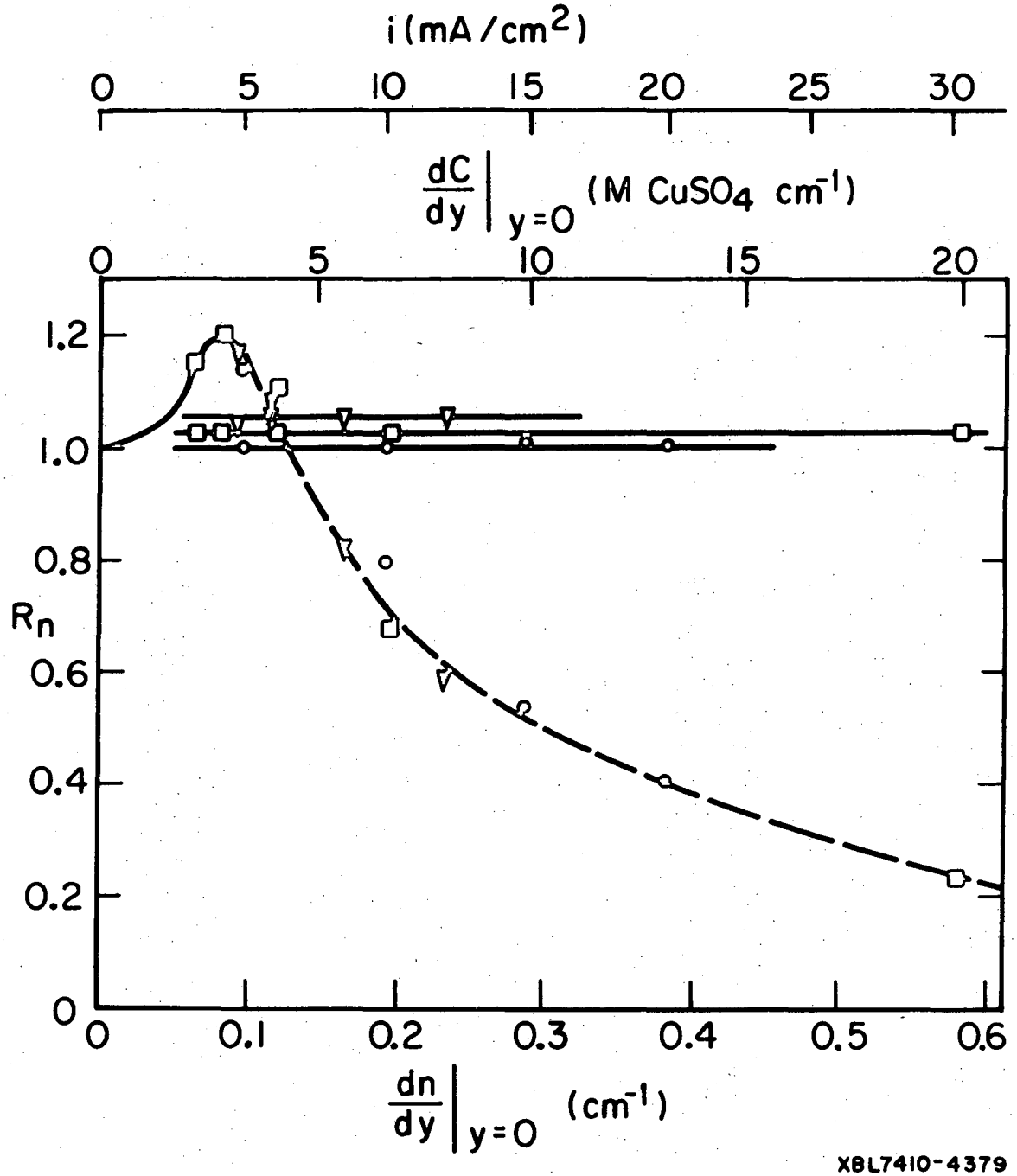
i (mA/cm²)
0
5
10
15
20
25
30
dC/dy | y=0 (M CuSO4 cm⁻¹)
0
5
10
15
20
1.2
1.0
0.8
Rn
0.6
0.4
0.2
0
0
0.1
0.2
0.3
0.4
0.5
0.6
dn/dy | y=0 (cm⁻¹)
XBL7410-4379

Fig. 6

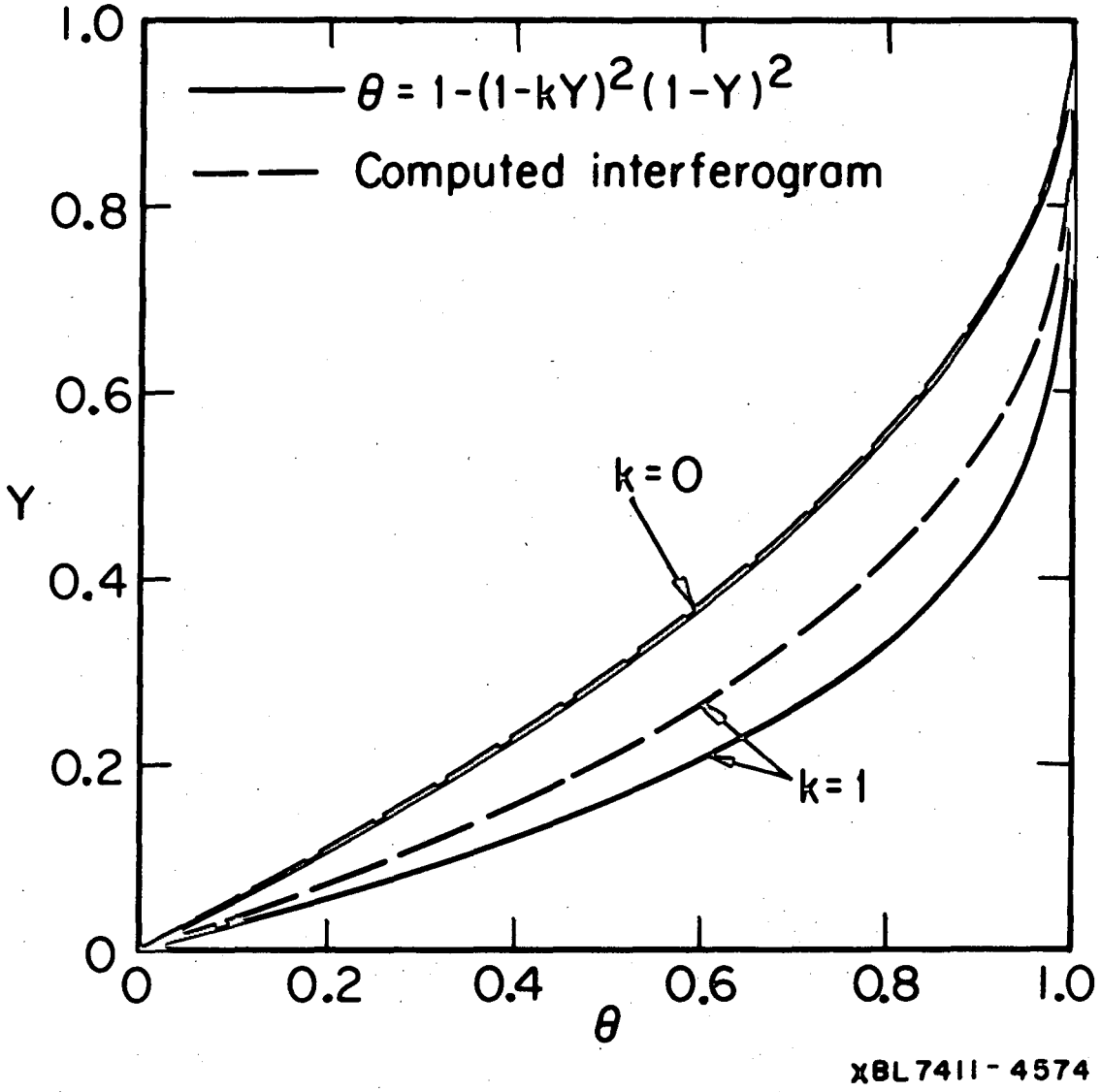
1.0
0.8
0.6
0.4
0.2
0
Y
0
0.2
0.4
0.6
0.8
1.0
θ
θ = 1-(1-kY)²(1-Y)²
Computed interferogram
k=0
k=1
XBL7411-4574

Fig. 7

TECHNICAL INFORMATION DIVISION
LAWRENCE BERKELEY LABORATORY
UNIVERSITY OF CALIFORNIA
BERKELEY, CALIFORNIA 94720